

**SAE TECHNICAL  
PAPER SERIES**

**1999-01-0454**

---

# **CFD Prediction and Experimental Validation of High-Temperature Thermal Behavior in Catalytic Converters**

**William Taylor III**  
Arvin Industries

**Reprinted From: Gas Direct Injection Aftertreatment and Exhaust Aftertreatment Modeling  
(SP-1455)**



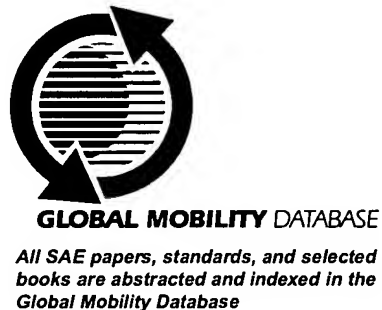
**International Congress and Exposition  
Detroit, Michigan  
March 1-4, 1999**

The appearance of this ISSN code at the bottom of this page indicates SAE's consent that copies of the paper may be made for personal or internal use of specific clients. This consent is given on the condition, however, that the copier pay a \$7.00 per article copy fee through the Copyright Clearance Center, Inc. Operations Center, 222 Rosewood Drive, Danvers, MA 01923 for copying beyond that permitted by Sections 107 or 108 of the U.S. Copyright Law. This consent does not extend to other kinds of copying such as copying for general distribution, for advertising or promotional purposes, for creating new collective works, or for resale.

SAE routinely stocks printed papers for a period of three years following date of publication. Direct your orders to SAE Customer Sales and Satisfaction Department.

Quantity reprint rates can be obtained from the Customer Sales and Satisfaction Department.

To request permission to reprint a technical paper or permission to use copyrighted SAE publications in other works, contact the SAE Publications Group.



No part of this publication may be reproduced in any form, in an electronic retrieval system or otherwise, without the prior written permission of the publisher.

**ISSN 0148-7191**  
**Copyright 1999 Society of Automotive Engineers, Inc.**

Positions and opinions advanced in this paper are those of the author(s) and not necessarily those of SAE. The author is solely responsible for the content of the paper. A process is available by which discussions will be printed with the paper if it is published in SAE Transactions. For permission to publish this paper in full or in part, contact the SAE Publications Group.

Persons wishing to submit papers to be considered for presentation or publication through SAE should send the manuscript or a 300 word abstract of a proposed manuscript to: Secretary, Engineering Meetings Board, SAE.

**Printed in USA**

# CFD Prediction and Experimental Validation of High-Temperature Thermal Behavior in Catalytic Converters

**William Taylor III**  
Arvin Industries

Copyright © 1999 Society of Automotive Engineers, Inc.

## ABSTRACT

A comprehensive CFD-based modeling approach is applied to several automotive catalytic converters, with the objective of predicting thermal behavior under steady-state, high-load conditions. Specialized computational models are used to account for effects of heat and mass transfer in the monolith, oxidation reactions, heat generation, conjugate heat transfer in the various converter materials, and radiation heat transfer. These various physical considerations are assembled in a comprehensive CFD model, which is solved using state-of-the-art computational techniques. Detailed temperature measurements, taken in engine-cell experiments at Ohio State University's Center for Automotive Research, are used to validate the CFD models. Excellent agreement seen between measured and computed temperatures, both inside the converter assembly and on the outer shell. Trends in the predictions and experiments are discussed, with the aim of understanding the physical mechanisms of heat transfer in monolithic catalytic converters. An increased understanding of these heat transfer mechanisms can be used to improve converter durability at high temperatures.

## INTRODUCTION

Temperature behavior is an important consideration in exhaust system design. Numerical methods, including computational fluid dynamics (CFD), are often employed to predict temperatures of exhaust systems, including catalytic converters. Temperature predictions are used to predict mounting system durability, to assure the viability of converter location relative to heat-sensitive components, and as input to structural finite-element analysis. In catalytic converter flows, numerical techniques are made more complex by the presence of chemical reaction and heat generation in the converter monolith. In addition to chemical reaction, catalytic converters include such features as porous media flow, conjugate heat transfer between materials of various properties, and thermal radiation heat transfer at high temperatures.

Specialized computational methods are required to deal with these effects in a numerical simulation.

Thermal studies of catalytic converters have been performed in the past, often with the objective of predicting emissions and thermal performance in transient situations. Early work by Young and Findlayson (1) and Sherony and Solbrig (2), among others, treated the problem of heat and mass transfer in monolith channels using analytical methods. Voltz et al. (3) first proposed oxidation rate equations for carbon monoxide and propylene on platinum-washcoated monolith channel walls. These equations are used in a variety of converter light-off studies. Using these reaction rate expressions, Heck et al. (4), among others, investigated heat & mass transfer with reaction kinetics in a single monolith channel. Oh and Cavendish (5) extended the method to investigate catalyst overheating problems under transient driving conditions. 1-D methods based on the same reaction rates and heat & mass transfer relationships are used extensively in the literature; see for example Siemund et al. (6) and Schweich (7).

The results obtained in single-channel studies were extended to two spatial dimensions, including the effects of a non-adiabatic wall boundary, by Chen et al. (8). The computed results were used to predict severe thermal gradients in the monolith, which have been shown to lead to monolith cracking problems. In a similar study, the method was extended from platinum-only catalysts to platinum/rhodium "three-way" catalysts by Chen and Cole (9). The multi-dimensional nature of these studies make them useful for predicting temperature fields, which can have a significant impact on mat erosion, shell deformation, and monolith cracking.

In the above-listed cases, constitutive equations are applied only to the monolith region, and not to the exhaust gas flow upstream and downstream of the catalyst. Velocity distribution across the monolith cross-section has been either an assumed function or assumed to be uniform at the monolith inlet. The relationship between monolith flow distribution and total pressure loss has been studied in some detail however, experimentally

by Wendland et al. (10, 11), and computationally by Benjamin et al. (12), Weltens et al. (13) and Lai et al. (14). These studies investigate the effects of inlet cone angle and substrate geometry on such performance parameters as monolith flow distribution and backpressure.

Generally speaking, the flow-related computational work in the open literature ignores heat generation effects of oxidation reactions. Conversely, computations which aim to predict reaction kinetics and exothermic behavior in converter monoliths often neglect effects of flow outside the monolith itself. In order to fully understand the consequences of converter design, a model must be formulated to include both sides of the problem; both reaction-based heat transfer and fluid flow.

The current work incorporates a fully three-dimensional treatment of all the relevant flow and heat transfer phenomena in catalytic converters, including:

- heat & mass transfer between the monolith solid & exhaust gas;
- oxidation reactions of carbon monoxide, propylene, and methane, and associated heat generation;
- 3-D Navier-Stokes equation treatment of flow upstream and downstream of the monolith;
- laminar anisotropic porous media treatment of flow in the monolith;
- 3-D, fully conjugate heat transfer in the monolith, insulating mat, and converter shell;

This comprehensive modeling methodology is applied to three different converter designs. Each design is simulated at two different high-temperature, steady-state engine conditions, such as would be used in converter durability tests. The results are compared to corresponding engine cell experiments in order to validate the computational method. Of special interest here are temperature fields in the catalytic converter. Predicted and measured pressure loss and conversion performance data are also presented.

## PHYSICAL MODELS

**POROUS MEDIA FLOW** – The governing equations of flow and heat transfer in a catalytic converter can be divided into two general categories: those equations which apply in the monolith brick itself, and those which apply in the regions outside the monolith. In the monolith, flow is assumed to be laminar and unidirectional along the converter axis (defined here as the z-axis in Cartesian coordinates). Neglecting entry effects, pressure loss in a monolith channel is given by Shah and London (15) as

$$\frac{\Delta P}{\rho V_z^2 / 2} = (f \text{Re})(4z^+) \quad (1)$$

which can be rearranged as

$$\frac{\Delta P}{\Delta z} = \frac{2\mu(f \text{Re})}{d_h^2} V_z \quad (2)$$

The friction factor  $f$  times channel Reynolds number  $\text{Re}$  is a constant quantity which changes only with cross-sectional shape. For a square-channel cross section,  $(f\text{Re}) = 14.227$  (ref. 15).

**MONOLITH ENERGY CONSERVATION** – The energy conservation equation for the fluid is related to the energy conservation equation for the solid using the local source term

$$S_1 = ha_s(T_s - T_f) \quad (3)$$

such that in the fluid at steady-state;

$$\rho_g c_p V_z \frac{dT_f}{dz} = ha_s(T_s - T_f) \quad (4)$$

Note that equation 4 does not consider heat diffusion across individual fluid channels in the x and y directions. This simplification is often made (8,9) because the diffusion is dominated by the surface interchange term on the right hand side of equation [4]. Put another way, the heat flux between solid and fluid described by equation [3] is far greater than the heat flux across a fluid channel diameter: the latter is therefore neglected.

In the monolith solid, the heat conduction equation is

$$(1 - \alpha) \left( \lambda_x \frac{\partial^2 T_s}{\partial x^2} + \lambda_y \frac{\partial^2 T_s}{\partial y^2} + \lambda_z \frac{\partial^2 T_s}{\partial z^2} \right) = ha_s(T_f - T_s) + \alpha_{p_i} \sum_{i=1}^{i=3} -\Delta H_i R_i \quad (5)$$

Note that the solid conductivity  $\lambda$  is anisotropic due to the monolith structure of the solid.

**CHEMICAL REACTION AND HEAT RELEASE** – The final term in equation 5 represents the heat of oxidation reaction for carbon monoxide (CO), propylene ( $\text{C}_3\text{H}_6$ ), and methane ( $\text{CH}_4$ ). Carbon monoxide is well known to be a prime contributor to heat generation in the monolith. The combination of propylene and methane is meant to simulate the presence of unburned hydrocarbons. These two species have been used in the past to represent unburned hydrocarbons (ref. 5), recognizing that many hydrocarbon species are typically present in real exhaust gas. The oxidation of these species is assumed to take place on the surface of the monolith channels, once the reacting species have been transferred from the gas phase to the solid phase. Reaction rates  $R_i$  are functions of local temperature and surface concentrations

$$R_i = \frac{k_i C_{si} C_{sO_2}}{G} \quad (6)$$

where

$$G = T(1 + K_1 c_{co} + K_2 c_{C3H6})^2 (1 + K_3 c_{co}^2 c_{C3H6}^2) (1 + K_4 c_{NO}^{0.7})$$

$$K_1 = k_{co} = (6.699 \times 10^{13}) \exp(-12556/T)$$

$$K_2 = k_{C3H6} = (1.329 \times 10^{15}) \exp(-14556/T)$$

$$K_3 = k_{CH4} = (7.326 \times 10^{10}) \exp(-19000/T)$$

$$K_4 = 65.5 \exp(961/T) \quad (6A)$$

$$K_2 = 2080 \exp(361/T)$$

$$K_3 = 3.98 \exp(11611/T)$$

$$K_4 = 479000 \exp(-3733/T)$$

**MONOLITH HEAT AND MASS TRANSFER** – Mass transport equations, analogous to the thermal balance of equation 4, are used to represent species diffusion from the gas to the solid in the channels;

$$V_z \frac{dc_f}{dz} = m_{mi} a_s (c_{fi} - c_{si}) \quad (7)$$

In equations 4 and 7, local heat and mass transfer coefficients ( $h$  in equation 3 and  $m_m$  in equation 7) can be estimated using one of several existing relationships. Shah and London (15) give the following relationship for laminar flow in square cross-section channels;

$$Nu \equiv \frac{hd_h}{\lambda_f} = 2.97 \quad (8)$$

which can be used to evaluate the channel heat transfer coefficient  $h$ . Equation 8 can be extended to the corresponding mass transfer relationship;

$$Sh \equiv \frac{m_{mi} d_h}{D_{mi}} = 2.97 \quad (9)$$

which can be used to find mass-transfer coefficient  $m_{mi}$ . It should be noted that, although the reaction rate expressions are more complex, it will be the Sherwood number which limits the reactions in the cases performed here. At high temperatures, the reaction is said to be mass-transfer limited, and will proceed almost instantaneously once species transfer has been made from the fluid to the solid phase. The constant values used here are chosen for their theoretical soundness and ease of implementation. Though more detailed expressions for  $Nu$  and  $Sh$  are the subject of much investigation (16,17), the determination of such expressions are beyond the scope of this report.

Outside the monolith, flow is governed by the Navier-Stokes equations in three dimensions. The heat conduction equation is used to represent the heat conduction in the shell and insulating mat.

## CFD METHODOLOGY

**SUMMARY OF CASES** – Three catalytic converter designs are chosen for the study, as listed in Table 1. In case 1, the catalytic converter monolith is not wash-coated, and therefore does not include significant chemical reaction. (In the experiments, an active, washcoated converter is inserted upstream of the test converter in case 1 in order to ensure that no reactants are present in the test piece). Case 1 is meant to evaluate the heat-transfer model without any reaction or exothermic behavior. Case 2 uses the same converter geometry as case 1, but in case 2 the monolith has been treated with a platinum-impregnated washcoat. Case 2 will therefore include significant chemical reaction and heat generation. In case 3 the converter design is significantly different. There are now two separate monoliths of oval cross-section, and there is no insulating mat in the cones or between the two monoliths. The washcoat in case 3 is equivalent to the washcoat in Case 2.

Each case listed above is simulated and tested at two engine conditions in order to thoroughly validate the modeling methodology across a range of temperatures. The two engine conditions are referred to as M for medium, H for high. So for example, the case 2 converter using the high engine condition will be referred to as case 2H. Various cases performed are summarized in Table 1. Sketches showing the internal layout of the converters are shown in Figure 1.

The converter materials are typical of current technology in use in the automotive industry, including vermiculite-based expanding mat mount material, 409 stainless steel shell, and ceramic 400cell/in<sup>2</sup> substrate. Because the reaction rate expressions given by equation [6] are for a platinum-only catalyst coating, and because this is a validation exercise, the coating on the active substrates is platinum-only, as opposed to a more typical platinum/rhodium or palladium formulation. (Expressions for Pt-Pd-Rh combinations to be used in the place of eqn. [6] are scant in the literature, and development of such expressions are beyond the scope of this report.)

Table 1: Summary of Cases

case	cross-section	number of monoliths	washcoat	engine condition
1M	round	1*	none	medium
1H	round	1*	none	high
2M	round	1*	35 g/ft <sup>3</sup> Pt	medium
2H	round	1*	35 g/ft <sup>3</sup> Pt	high
3M	oval	2	35 g/ft <sup>3</sup> Pt	medium
3H	oval	2	35 g/ft <sup>3</sup> Pt	high

\* two monoliths adjacent to each other(i.e. butted-up)

will be treated as a single monolith

**COMPUTATIONAL MODELS** – A computational grid is generated for each of the six cases to be studied using ICEM-CFD's Hexa grid generation software. Each grid is composed of approximately 310,000 hexahedral cells, representing a quarter-symmetry geometry of each converter. The mat and converter shell are both represented by 3-D hexahedral cells. The grids are shown in Figure 2. Note that Figure 2 shows only the part of the grid composing the converters: the grid extends upstream, out of the range of Figure 2, to represent the inlet pipe section.

The equations of flow are discretized using the self-filtered central-differencing scheme (SFCD). This second-order scheme offered the best combination of robustness and accuracy for this class of cases. The standard k- $\epsilon$  turbulence model is used to account for turbulent fluctuations. In the near-wall region, the low Reynolds number k- $\epsilon$  model of Norris and Reynolds (18) is applied. This "two-layer" turbulence modeling approach is often more accurate in representing near-wall turbulent flow behavior and has been recommended for use in this class of flows (12,19).

The CFD practices listed briefly here are based on recommendations of the literature, experience in CFD modeling, and a rigid interpretation of CFD guidelines. Every attempt was made to avoid common deficiencies in the open literature such as coarse or skewed grids, incomplete computational domains, diffusive first-order discretization schemes, and unsuitable turbulence modeling practices. The simulations here attempt to be of the highest quality in all aspects of general CFD practice before consideration of the specialized models for mass transfer, reaction, etc.

User subroutines are required to perform the following tasks in the CFD simulations;

- Solve for fluid and solid species concentrations in the monolith. At each cell location in the monolith, user

subroutines equate the mass transfer rate (from fluid to solid phase) with the reaction rate in the solid phase (i.e., the elimination of reactant mass in the solid phase);

- Generate heat in the solid phase, and transfer heat between solid and fluid phases in the monolith;
- Calculate a local resistance to flow using the local temperature-dependent laminar viscosity and equation [2].

The Star-CD user subroutines to carry out these operations have been developed by Clarkson (20, 21). These subroutines, modified slightly where necessary are used in this study.

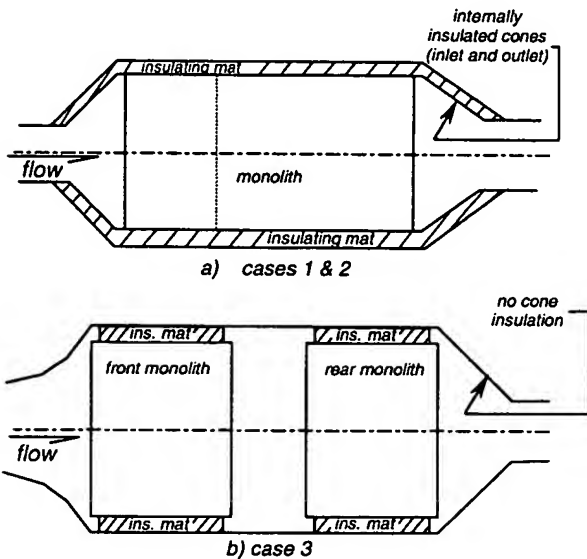


Figure 1. Catalytic Converter Geometry Cross-Sectional Views

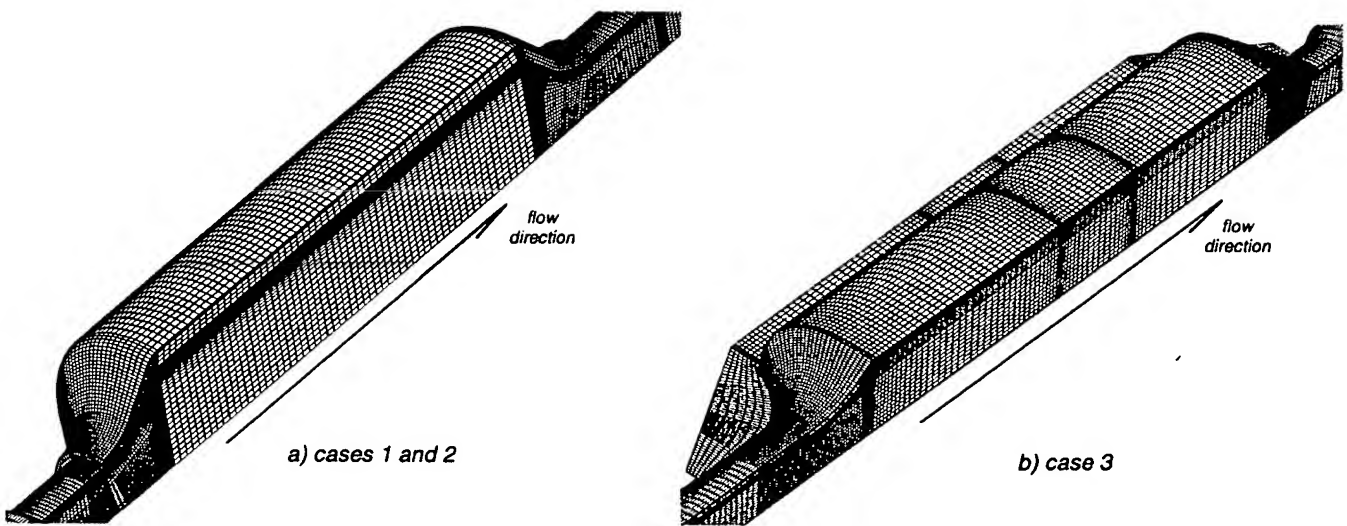


Figure 2. CFD Computational Grids

**BOUNDARY CONDITIONS** – For this type of validation study, it is imperative that the conditions assigned to the computations match the conditions seen in the experiments. Boundary conditions for inlet mass flow, temperature, and species concentrations are therefore assigned to match experimental measurements as exactly as possible. This boundary-condition matching leads to CFD boundary conditions which vary slightly from case to case, since the engine-cell experiments vary slightly from case to case. A summary of boundary conditions is given in Table 2.

Table 2: CFD Boundary Conditions

inlet	case					
	1M	1H	2M	2H	3M	3H
velocity (m/s)	65.1	82.8	64.6	116.8	64	107.2
temperature (C)	768	803	738	829	727	824
inlet CO (vol %)	-	-	0.94	0.93	1.01	0.31
inlet total HC (ppm)	-	-	677	394	942	392
inlet O2 (vol %)	-	-	0.33	0.18	0.39	0.21
turbulence	5% turbulence intensity @ 5mm length scale					
<b>ambient wall</b>						
film coeff (W/m <sup>2</sup> )	20	20	20	20	20	20
temperature(C)	303	303	303	303	303	303
shell emissivity	0.3	0.3	0.3	0.3	0.3	0.3

- inlet conditions based on measured data (turbulence is estimated)

- constant inlet velocity and temperature profiles are allowed to develop over long computational inlet length

- ambient conditions estimated based on straight-pipe temperature measurements

**MATERIAL PROPERTIES** – A variety of approaches are required to calculate material properties. The gas properties are dependent on temperature but not gas composition, an assumption acceptable when the reacting species compose only a small fraction of the overall flow. This is referred to as a “passive – contaminant” approach. A summary of material property calculations and assumptions are listed in Table 3.

Table 3 : Material Properties

<b>monolith</b>	
<i>material</i>	<i>cordierite ceramic</i>
<i>cell density</i>	<i>400cpsi/6.5 thickness</i>
<i>coating</i>	<i>Pt-only</i>
<b>gas</b>	
<i>material</i>	<i>86% N<sub>2</sub> , 14% CO<sub>2</sub></i>
<i>density</i>	<i>ideal gas law</i>
<i>viscosity</i>	<i>Sutherland's formula</i>
<i>thermal conductivity</i>	<i>polynomial function</i>
<i>mass diffusivity</i>	<i>reference (22), pg. 505</i>
<i>molecular weight</i>	<i>30.3</i>
	<i>(gas properties are not influenced by reaction)</i>
<b>shell</b>	
<i>material</i>	<i>409 stainless steel</i>
<i>thermal conductivity</i>	<i>constant 27W/m<sup>2</sup></i>
<b>mat</b>	
<i>material</i>	<i>intumescing expanding mat</i>
<i>thermal conductivity</i>	<i>polynomial fit (based on manufacturers data)</i>

Star-CD version 3.0c is the CFD software used to assemble and solve the problem. The solutions require approximately 800 iterations to converge. Approximate solution time is 36 hours on a Sun Ultra2. Table 4 lists several pertinent computational parameters.

Table 4: CFD Solution Parameters

<b>grid size</b>	310,000 cells
<b>grid type</b>	all hexahedral, structured-type grid
<b>discretization</b>	self-filtered central differencing
<b>solution algorithm</b>	SIMPLE
<b>convergence</b>	normalized residuals<1e-3 (norm.residuals decrease 3 orders of magnitude for k, ε equations)
<b>approx. run time</b>	36 hrs/case

## EXPERIMENTAL METHOD

Validation experiments were performed in an engine cell at Ohio State University's Center for Automotive Research. A sketch of the experimental system is shown in Figure 3. Note that in cases 1M and 1H, where the test piece is not washcoated with catalyst material, an active, washcoated catalytic converter is placed in the exhaust gas stream upstream of the test piece. This is done to clean the exhaust gas of any species which might otherwise react in the test piece. In the remaining cases, the non-instrumented converter is replaced by a straight pipe. Experimental data was taken after the system had reached steady-state for a given engine condition. The following variables were recorded;

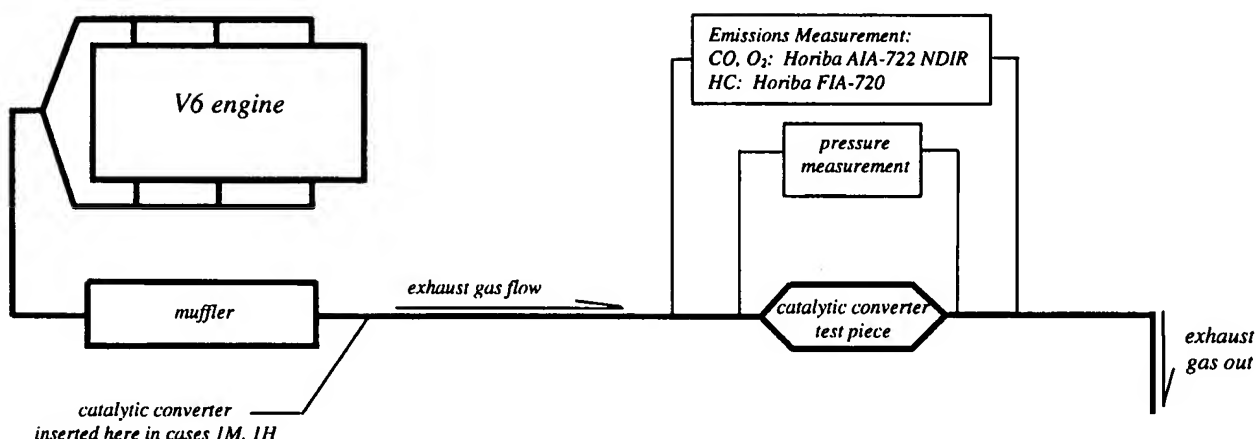
- gasoline flow rate;
- air/fuel ratio;
- species concentrations of CO, O<sub>2</sub>, CO<sub>2</sub>, NO<sub>x</sub>, and hydrocarbons, upstream and downstream of the catalyst;
- temperatures on the converter shell;
- temperatures in the converter bricks;
- pressure upstream and downstream of the catalyst;

- gas temperature upstream and downstream of the catalyst.

A diagram showing the system layout is shown in Figure 3. The silencing element is inserted upstream of the converter to suppress severe pressure fluctuations which can affect the catalyst flow & heat transfer behavior. Temperatures were measured on the converter shells and inside the monoliths using K-type thermocouples. The locations for temperature measurements are shown in Figure 4 for the round converters (cases 1 and 2) and in Figure 5 for the oval converter (case 3).

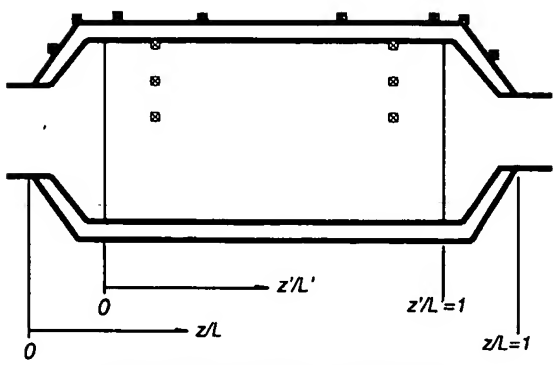
Some notation which will be used to describe the results is shown in Figures 4 and 5;

- z/L – measured axially from the beginning of the converter shell, such that z/L = 0 at the beginning of the inlet cone and z/L = 1 at the end of the outlet cone;
- z'/L' – measured axially from the beginning of the front substrate, such that z'/L'=0 at the monolith front face and z'/L'=1 at the monolith rear face;
- r/R<sub>mw</sub> - measured radially from the center of the converter such that r/R<sub>mw</sub>= 0 at the monolith center and r/R<sub>mw</sub>=1 at the monolith outer radius.

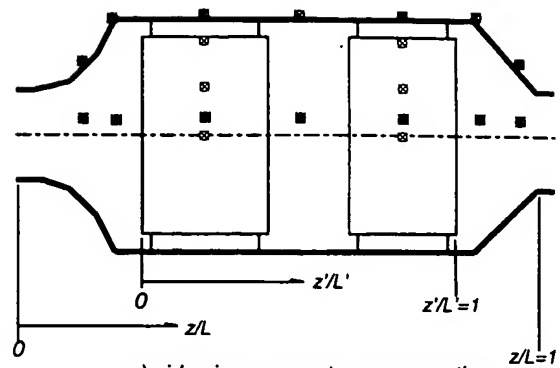


<b>estimated uncertainty</b>	
mass flow rate (velocity)	+/- 8%
emissions species	+/- 1.5%
temperature	+/- 0.75% (7-9 C)

Figure 3. Experimental Exhaust System

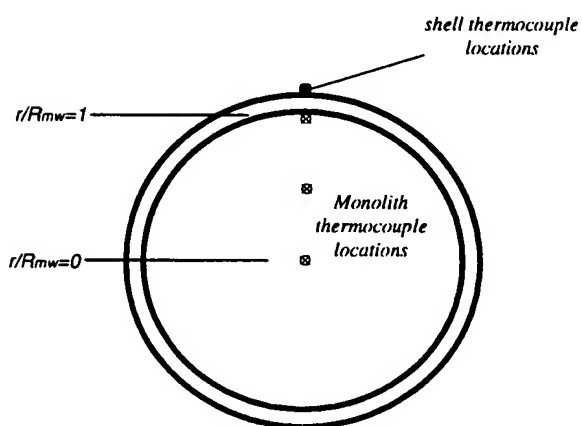


a) side view, converter cross-section



a) side view, converter cross-section

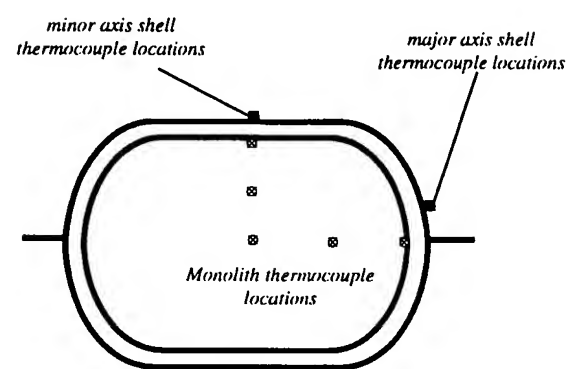
■ - shell thermocouple  
□ - monolith thermocouple



b) front view – converter cross-section

Figure 4. Thermocouple Locations, Cases 1 and 2

■ - shell thermocouple  
□ - monolith thermocouple



b) front view, case 3 converter cross-section

Figure 5. Thermocouple Locations, Case 3

## RESULTS AND DISCUSSION

PRESSURE LOSS – Table 5 lists predicted versus measured pressure loss for all six cases. Pressure loss is underpredicted in cases 1 and 2, but overpredicted in case 3. There are several possible reasons for discrepancies in pressure loss predictions, including

- uncertainty in monolith channel diameter;
- uncertainty in the A/F ratio, which is used (along with fuel-flow measurements) to calculate the inlet mass flow rate of the CFD cases;
- discretization and numerical error (e.g., numerical diffusion);
- turbulence modeling inaccuracies;
- transient effects of flow pulsations.

**Table 5: Pressure Loss Results**

case	Pressure Loss (kPa)		
	measured	computed	% difference
1M	10.8	9.35	-14.4%
1H	15.81	12.53	-23.1%
2M	11.71	11.17	-4.7%
2H	20.89	18.56	-11.8%
3M	8.63	11.43	27.9%
3H	16.18	18.5	13.4%

CONVERSION – Table 6 lists conversion efficiencies for CO and total hydrocarbons for all six cases. Hydrocarbon efficiencies are fairly accurate in all cases; carbon monoxide efficiencies are underpredicted in all cases. A probable reason for the consistent CO underprediction is the lack of NO<sub>x</sub> chemistry in the computations. In the experiment, significant NO<sub>x</sub> reduction takes place, which supplies further oxygen to continue the CO oxidation reaction.

It should be noted that the catalytic converters in this study are not designed for use with the test engine, nor is the engine controlled for optimum use with the converters. Therefore complete conversion is not expected. In all cases, it is lack of excess oxygen which keeps the pollutant species from completely oxidizing.

**Table 6: Conversion Results**

case	species	conversion efficiency (%)	
		measured	computed
2M	CO	71	55
	HC-total	71	74
2H	CO	47	33
	HC-total	71	64
3M	CO	84	59
	HC-total	77	70
3H	CO	65	40
	HC-total	76	69

TEMPERATURE: CASES 1M AND 1H – Figures 6 and 7 show measured versus computed temperature profiles in cases 1M and 1H, respectively. Because there is no reaction in cases 1M and 1H, no increase is seen in gas temperatures as flow moves through the monolith. In both cases, shell temperatures are significantly cooler than gas temperatures, especially in the monolith region. On the inlet cone, steep axial temperature gradients are seen, decreasing shell temperatures by several hundred degrees over the length of the cone. A similar profile is seen on the outlet cone.

The temperature profile entering the monolith is non-uniform due to flow and temperature patterns in the inlet cone. Computed temperature contours showing this pattern at the monolith entrance are shown in Figure 8. A hot core temperature, which has not been significantly affected by thermal boundary layers in the inlet pipe and cone, forms the high-temperature core flow in the center of the monolith. Fluid which has been cooled somewhat by thermal boundary layers in the inlet pipe and cone enters the monolith near the outer radius. At the inlet monolith face ( $z'/L' = 0$ ), the predicted temperature difference between the centerline and outer radius is approximately 50 degrees C in cases 1M and 70 degrees C in case 1H. Similar temperature differences are seen in the measurements at  $z'/L'=0.125$ .

The lower-temperature region near the monolith outer radius grows along the length of the monolith until it reaches the monolith exit. In the monolith, the layer is best described as a conduction layer, as it is maintained by radial conduction through the insulating mat. Although the conduction layer continues to grow along the length of the monolith, it is more significantly impacted by the inlet temperature profile than by radial conduction in cases 1M and 1H. In case 1H for example, the temperature difference ( $T_{cl} - T_{mw}$ ) which is a maximum at the monolith outlet, has already reached 60% of its maximum value at the monolith inlet. In cases 1M and 1H then, monolith temperature profiles are affected more significantly by flow in the inlet cones than by radial diffusion.

The influence of the conduction layer is apparent in the measured and computed shell temperature shown in Figures 6 and 7. Shell temperatures decrease to a minimum at approximately  $z'/L' = .75$ , or  $\frac{3}{4}$  along the length of the monolith. The decrease is due to the decreasing radial heat flux from the monolith as the conduction layer grows and radial temperature gradients in the monolith and mat become less severe. At around  $z'/L' = .75$ , axial conduction from the outlet cone shell begins to have a significant impact on shell temperature, and the shell temperature rises again.

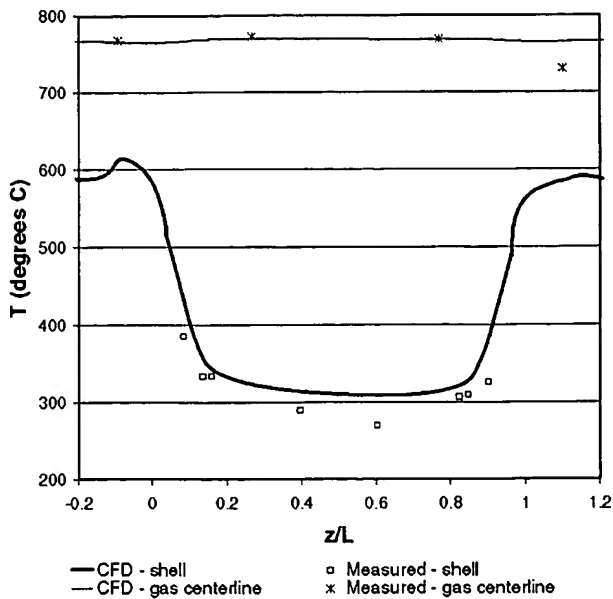


Figure 6. Temperature Profiles, Case 1M

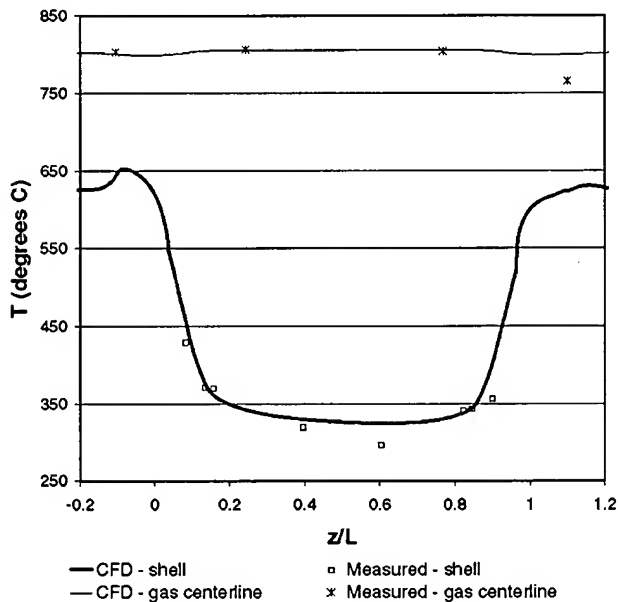


Figure 7. Temperature Profiles, Case 1H

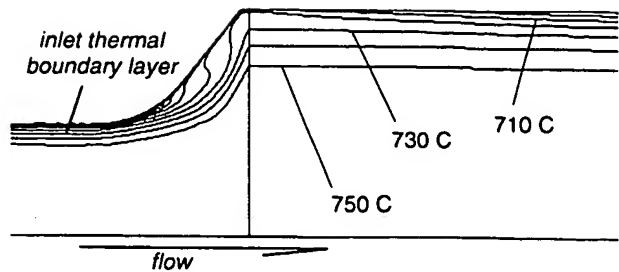


Figure 8. Temperature Contours in the Inlet Cone of Case 1M (side view, cross-section)

**TEMPERATURE:CASES 2M AND 2H** – Figures 9 and 10 show measured versus computed temperature profiles in cases 2M and 2H, respectively. An increase in measured gas temperature of 62 and 37 degrees is seen in the monolith of cases 2M and 2H, respectively. Similar temperature gains are seen in the computations, as shown in Figures 9 and 10. This gas temperature increase is due to the heat of reaction for the three reactions considered. Under the high-temperature conditions considered here, the reactions take place over the first several centimeters of the front monolith, between  $z'/L'=0$  and  $z'/L'=0.2$ . Methane oxidation is an exception; however, this reaction generates an insignificant amount of heat compared to the other reactions considered.

Note that there is more heat generated in case 2M than in 2H, although overall temperature levels are greater in case 2H. This behavior is due to the engine control scheme, which runs slightly rich at higher loads. Rich A/F ratios decrease O<sub>2</sub> levels in the exhaust, leading in turn to less complete conversion in the higher-load 2H case. The same trend is seen in cases 3M and 3H.

Unlike in case 1, in case 2 there is a significant difference between the monolith solid and fluid temperatures between  $z'/L' = 0$  and  $z'/L' = .5$ . These monolith temperature profiles in case 2H are shown in Figure 11. Solid temperature reaches a maximum immediately at the inlet face of the monolith. There is however a radial temperature distribution across the monolith solid front face. In case 2H for example,  $[T_{cl} - T_{mw}]$  is in excess of 70 degrees C. A significant amount of heat is transferred from the monolith solid to the fluid in the channels between  $z'/L' = 0$  and  $z'/L' = 0.5$ . In this region, gas temperatures rise while solid temperatures fall, until the two become essentially equal around  $z'/L'=0.5$ .

The differences between solid and fluid temperatures in the monolith do not change the basic nature of the conduction layer at the monolith outer edge. It is still influ-

enced heavily by gas inlet temperature profile as well as radial diffusion in the monolith itself. This conduction layer is shown in Figure 12, a plot of radial temperature profiles in the monolith at two axial locations in case 2H. At  $z'/L'=1.25$ , both solid and fluid temperatures decrease significantly near the wall, although the solid profile is 30 degrees or so hotter than the fluid profile. At  $z'/L'=8.75$ , the solid and fluid temperatures are nearly identical. The significance of the monolith conduction layer and the exothermic reactions combine in Figure 12 to create an interesting fluid temperature field: centerline fluid temperature increases in the axial direction, while fluid temperature at  $r/R_{mw}=1$  decreases in the axial direction.

The monolith temperature profiles shown in Figure 11 lead to mat temperature maximums at the mat leading edge (at  $z'/L'=0$ ), adjacent to the monolith. It is here where the mat will first be pushed past its temperature limit in very-high temperature durability tests. As has been shown in case 2, this maximum mat temperature will be impacted significantly by chemical reaction and temperature distribution at the monolith inlet. Though a uniform flow distribution will improve backpressure and catalyst coating longevity, significant decreases in mat and shell temperatures can be realized by reducing flow in the outermost channels, i.e. as  $r/R_{mw}$  approaches 1. In the limit, elimination of flow in these channels would create a stagnant region without reaction or associated heat generation. Past work which has focused on the adverse effects of flow maldistribution in converter monoliths (12,13) does not consider the durability effects of reduced flow at the far outer radius of the monolith.

Shell temperature profiles between cases 1M and 2M look very similar. To better appreciate the difference between them, recall that the inlet gas temperature of case 2M is 30 degrees C cooler than case 1M. So the nearly equivalent computed shell temperatures in these two cases demonstrate the heating effect of the conversion reactions on shell temperatures. The temperature increases associated with chemical reaction are important when performing structural analysis of a catalytic converter assembly. Both mat properties and shell thermal stresses are heavily dependent on temperature. A major benefit of this type of analysis is its accurate prediction of mat and shell temperatures under reacting conditions, which can be used as input boundary conditions for structural finite element analysis.

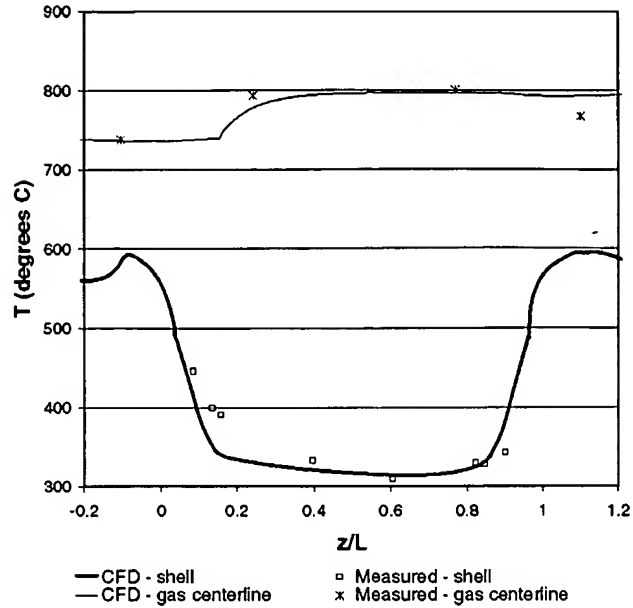


Figure 9. Temperature Profiles, Case 2M

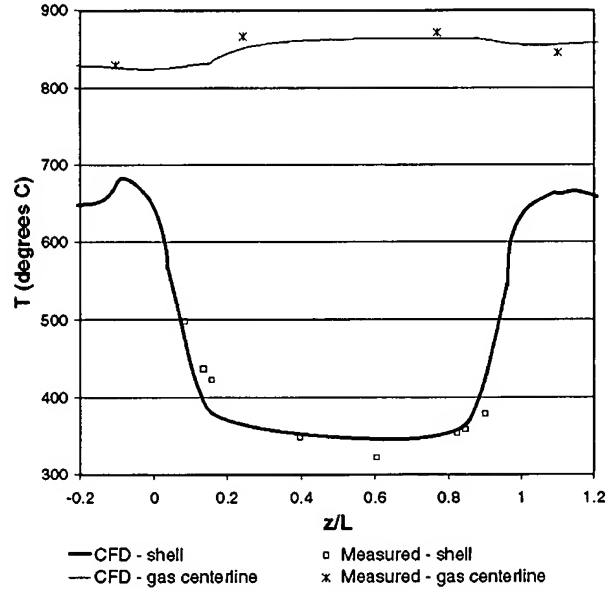


Figure 10. Temperature Profiles, Case 2H

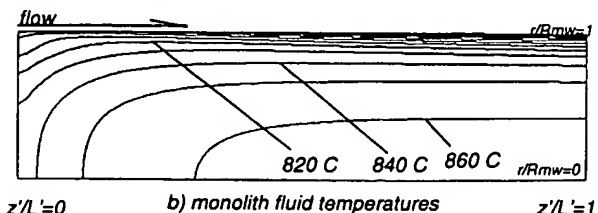
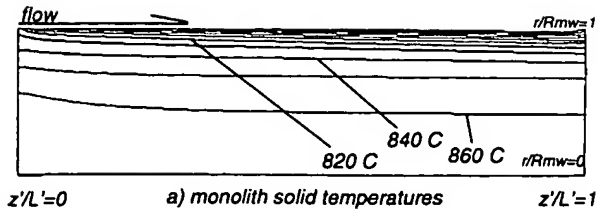


Figure 11. Monolith Solid and Fluid Temperature Contours in Case 2H (side view, cross-section)

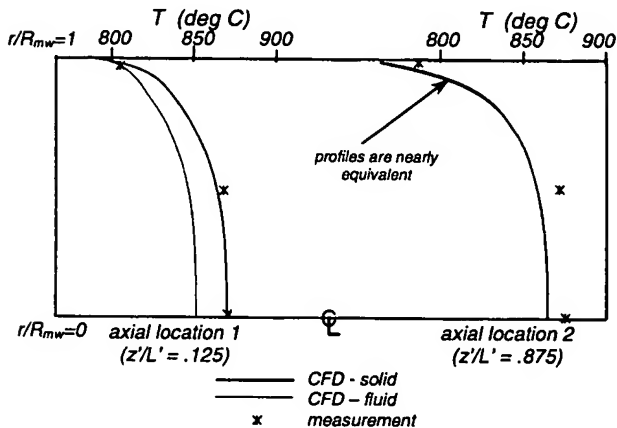


Figure 12. Monolith Conduction Layer Development in Case 2H

**TEMPERATURE: CASES 3M AND 3H** – Figures 13 and 14 show predicted and measured temperature profiles in cases 3M and 3H, respectively. Note that the shell temperature profile is significantly different from previous cases due to the different insulation strategy used in design 3 (reference Figure 1). Rapid axial decrease in shell temperature along the inlet cones is followed by a sudden rise at the mid-bed region, where the shell is not protected by insulation.

In all cases of steep axial temperature gradients on the shell, it is imperative to include 3-D cells representing the steel converter shell. Axial conduction through these elements controls temperature profiles in these critical high-solid-gradient regions. This axial conduction effect is crucial to the accurate prediction of mat-edge temperatures and shell temperature gradients, both of which are key predictors of converter durability.

In cases 3M and 3H temperatures at the monolith outer edge, and in the mat and shell, are significantly cooler at the cross-sectional major axis than the minor axis. Measured and computed temperatures are lower along the major axis than the minor axis by approximately 50C in case 3M and 70C in case 3H. This trend is seen everywhere except at the outlet cone shell, where computed major and minor axis shell temperatures approach each other.

This trend in shell temperatures can be traced to temperature profiles in the monolith. Cross-sectional monolith temperature profiles are shown in Figure 15. The differences between major and minor axis temperature levels is due in large part to flow effects in the inlet cone. As in cases 1 and 2, significant decreases in gas temperatures are seen in the thermal boundary layers of the inlet pipe and cone. These boundary layers lead to decreased temperatures entering the monolith near its outer edge, especially along the major axis where there is more severe separation, recirculation, and temperature degradation in the inlet cone. A secondary factor is the flange on the converter shell, where the top and bottom shells are welded together. The flange acts as a heat sink which conducts heat away from the monolith along the major axis.

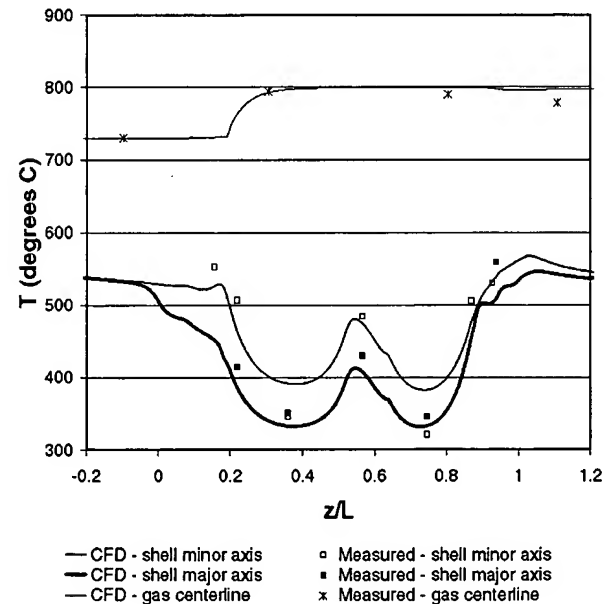


Figure 13. Temperature Profiles, Case 3M

The previously identified monolith conduction layer is interrupted in the mid-bed region (between the monoliths) in cases 3M and 3H. Temperature contours in this region are shown in Figure 16. The gas which contacts the shell in the mid-bed region is the same gas which has been cooled below the core temperature in the monolith conduction layer. Although heat transfer coefficients between the gas and mid-bed shell are high, the temper-

ature of the gas contacting the shell is lower than the centerline gas temperature by 100 degrees C or more. The shell is therefore protected from the maximum temperatures in the core flow. Although the conduction layer is interrupted by the gap between the monoliths, it continues in the second monolith without significant changes. The leading edge of the second mat is therefore also protected by the conduction layer in the mid-bed region.

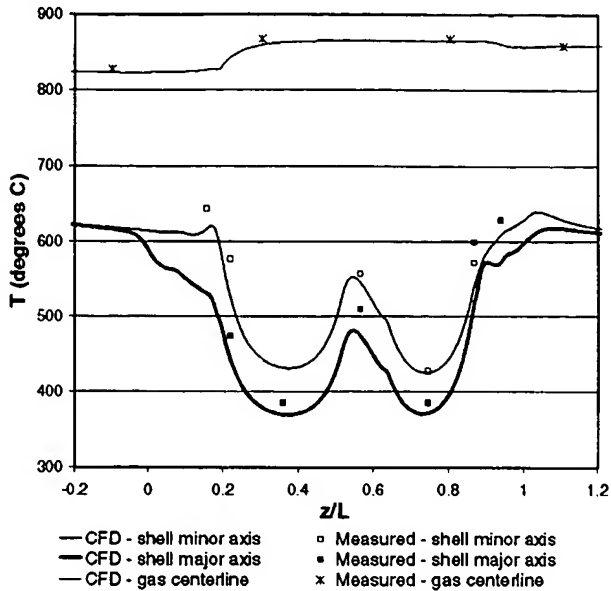
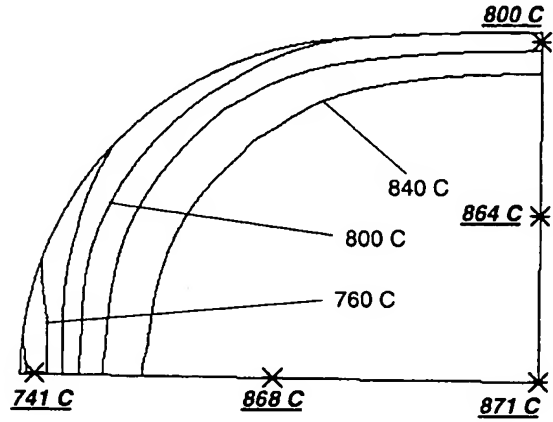


Figure 14. Temperature Profiles, Case 3H

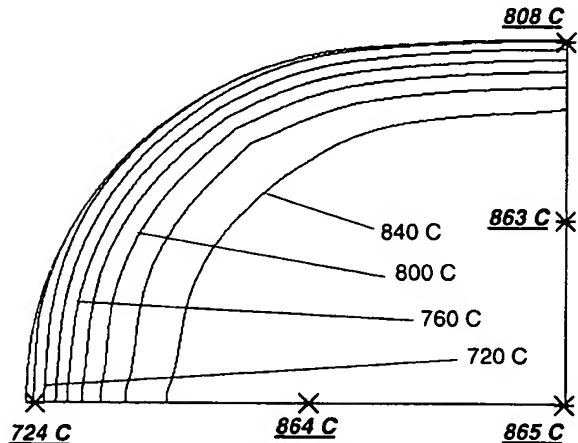
The conduction layer in the mid-bed region has significant impact on converter durability. Chen et al. (5) have proposed that more insulation leads to a more uniform radial temperature profile in the front monolith, leading in turn to reduced thermal gradients and thermal stresses in the rear section of the monolith. On the other hand, a more insulated design retains higher temperatures in the conduction layer, leading to higher shell temperatures in the mid-bed region. These higher shell temperatures can lead to excessive shell warpage, thus affecting the durability of the shell assembly. A tradeoff must be made which provides enough insulation to protect the monolith from transient thermal gradients without overheating the mid-bed shell.

Temperatures are significantly lower in the second mat due to the expanded conduction layer in the second monolith. Though the second mat will be less affected by high-temperature degradation, it will be more susceptible to low-temperature problems should they arise. Note for example in case 3M, where inlet gas approaches 730 degrees C, the shell over the second brick along the minor axis is not yet to the expansion temperature of the mat. Incomplete mat expansion can lead to problems in mat erosion and substrate retention. Low-temperature concerns are increasingly important as manufacturers move toward thicker mats in converter designs.

Fluid which contacts the outlet cone shell has been cooled in the monolith conduction layer. Here, as in the mid-bed region, the conduction layer (now better described as a thermal boundary layer) offers the shell some protection from the hotter core flow. However, the experiments show hotter temperatures on the outlet cone surface than do the predictions. Thermal radiation from the substrate rear face (not accounted for in the computations) may play a role in increasing cone shell temperatures, especially along the major axis where view factors between the two surfaces are highest.



a) midway through front monolith



b) midway through rear monolith

— 700 C : computed temperatures
* 700 C : measured temperatures

Figure 15. Temperaure Profiles on Monolith Cross-sections, Case 3H (front view)

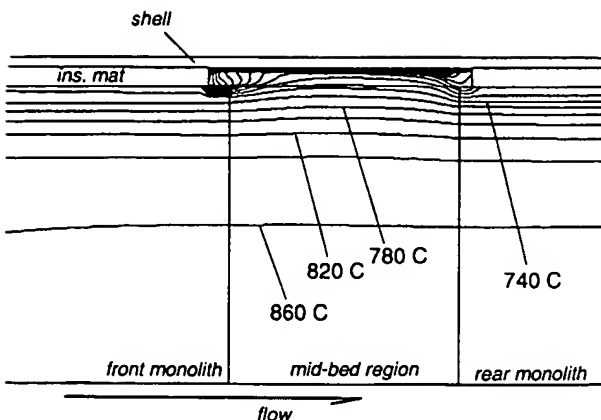


Figure 16. Temperature Profile in the Midbed Region of Case 3H (side view, major axis cross-section)

## CONCLUSIONS

Significant conclusions of the study are as follows:

1. A complete computational methodology has been established for prediction of catalytic converter thermal behavior under steady, high-load situations. The modeling method has been validated in 6 different cases.
2. A thermal conduction layer, formed by entrance effects in the converter inlet cone and enhanced by radial heat diffusion in the monolith, has a significant impact on temperature behavior in the mounting mat, shell, and monolith.
3. In the case of a dual-monolith, oval cross-section catalytic converter, significant variations in thermal behavior are seen along the major and minor axes. The mid-bed region also has a significant impact on shell and mat temperatures.
4. The results obtained in this study may be used to develop equations for temperature field behavior as a function of design parameters such as brick radius, mid-bed size, shell thickness, mat thickness, etc. Such equations will be useful as design guidelines to be used throughout the catalytic converter design process. These temperature results will also be used as input boundary conditions for structural finite element analysis to predict shell stress and deflection.

Currently, the heat transfer model is used extensively to assess the effects of particular design changes, such as upstream bends, cone geometry changes, etc., on durability performance. Future work will include the development of expressions noted in conclusion 4. Work is also underway to further enhance the computational model, especially, to include the effects of thermal radiation between the substrate faces and the shell cones. Though the computational method for this radiation calculation is in place and has been implemented with some success, the emissive properties of a converter substrate face are not yet well known.

## ACKNOWLEDGEMENTS

The author would like to thank Dr. Ahmet Selamet and his team at Ohio State University's Center for Automotive Research (CAR). Their help in planning and performing the experiments was instrumental to the success of this validation effort. Thanks also go to Rick Lyon and John Harris at Arvin, and Yale Jones at OSU, for their help in planning and producing the experimental system.

## REFERENCES

1. Young and Findlayson; "Mathematical Modeling of the Monolith Catalytic Converter – Part 1: Development of Model and Application of Orthogonal Collocation" *AIChE Journal*, 22 page 331, 1976.
2. Sherony and Solbrig, "Analytical Investigation of Heat and Mass Transfer Friction Factors in a Corrugated Duct Heat or Mass Exchanger," *International Journal of Heat and Mass Transfer*, vol 13, p1455, 1970.
3. Voltz, Morgan, Liederman, and Jacob; "Kinetic Study of Carbon Monoxide and Propylene Oxidation on a Platinum Catalyst." *Industrial and Engineering Chemistry: Product Research and Development*, vol. 12. No. 4, 1973.
4. Heck, Wei, and Katzer; "Mathematical Modeling of Automotive Catalysts" *AIChE Journal*, 22, page 447, 1976.
5. Oh and Cavendish; "Transients of Monolithic Catalytic Converters: Response to a Step Change in Free-Stream Temperatures as Related to Controlling Automobile Emissions," *Industrial and Engineering Chemistry: Product Research and Development*, Vol 21, p29, 1982.
6. Siemund, Schweich, Leclerc, and Villermoux, "Modeling 3-way Catalytic Converter: Comparison Between Simulation and Experimental Data," *Studies in Surface Science and Catalysis*, vol 96, Elsevier Science B.V., 1995.
7. Schweich, "Laboratory Data for Three-Way Catalytic Converter Modeling," *Studies in Surface Science and Catalysis*, Vol 96, Elsevier Science B.V., 1995.
8. Chen, Oh, Bishop, and Van Ostrom; "A Three-Dimensional Model for the Analysis of Transient Thermal and Conversion Characteristics of Monolithic Catalytic Converters," *SAE Paper 880282*, 1988.
9. Chen and Cole; "Numerical Simulation and Experimental Verification of Conversion and Thermal Responses for a Pt/Rh Metal Monolithic Converter," *SAE Paper 890798*, 1989.
10. Wendland and Matthes; "Visualization of Automotive Catalytic Converter Internal Flows," *SAE Paper 861554*, 1986.

11. Wendland, Sorrell, Kreucher, "Source of Monolithic Catalytic Converter Pressure Loss," SAE Paper 912372, 1991.
12. Benjamin, Clarkson, Haimad, and Grgis; "An Experimental and Predictive Study of the Flow Field in Axisymmetric Automotive Exhaust Catalyst Systems," SAE Paper 961208, 1996.
13. Weltens, Bressler, Terres, Neumaier, and Rammoser, "Optimisation of Catalytic Converter Gas Flow Distribution by CFD Prediction," SAE Paper 930790, 1993.
14. Lai, , Kim , Cheng, Chui, Pakko; "Three-Dimensional Simulations of Automotive Catalytic Converter Internal Flow," SAE Paper 910200, 1991.
15. Shah and London; "Laminar Forced Convection Heat Transfer and Flow Friction in Straight and Curved Ducts – A Summary of Analytical Solutions," Technical Report #75, Department of Mechanical Engineering, Stanford University, 1972.
16. Ullah, Waldram, Bennet, and Truex, "Monolithic Reactors: Mass Transfer under Reacting Conditions," Chemical Engineering Science, vol. 47, No. 9-11, page 2413.
17. Votruba, Mikus, Khue, Nguen, Hlavacek, and Skrivanek, "Heat and Mass Transfer in Honeycomb Catalysts II" Chemical Engineering Science, vol. 30, pp201-206.
18. Norris and Reynolds, "Turbulent Channel Flow With Moving Wavy Boundary," Report FM-10, Department of Mechanical Engineering, Stanford University.
19. Star-CD Users Manual, Version 3.0c, Computational Dynamics Limited, 1996.
20. Clarkson; "The Simulation of the Heat Transfer, Chemical Reactions and Fluid Flow Within a Catalytic Converter," Star-CD Internal Report, 1996.
21. Clarkson; "The Implementation of a Reacting Catalyst Model Within Star-CD," Star-CD Internal Report, 1996.
22. Bird, Stewart, and Lightfoot; Transport Phenomena, J. Wiley & Sons, New York, 1960.

## NOMENCLATURE

### VARIABLES

$a_s$ : monolith surface area per unit volume ( $m^2/m^3$ )  
 $a_{pt}$ : surface area of platinum per unit volume ( $m^2/m^3$ )  
 $C_p$ : specific heat (kg/kJ)  
 $C_{fi}$ : mole fraction of species  $i$  in fluid (mol/mol)  
 $c_{si}$ : mole fraction of species  $i$  in solid (mol/mol)  
 $d_h$ : hydraulic diameter (m)  
 $D_{mi}$ : mass diffusivity of species  $i$  in exhaust ( $m^2/s$ )  
 $f$ : laminar friction factor (-)  
 $h$ : heat transfer coefficient ( $W/m^2C$ )  
 $\Delta H_i$ : heat of reaction (J/mol)  
 $k_i$ : reaction rate constant for reaction  $i$  ( $mol/m_{pt}^2 s$ )  
 $m_{mi}$ : mass transfer coefficient for species  $i$  ( $kg/m^2 s$ )  
 $P$ : pressure (kPa)  
 $r$ : radial coordinate (m)  
 $R_i$ : specific reaction rate ( $mol/m^2 P_t s$ )  
 $S$ : convective source term ( $W/m^2$ )  
 $T$ : temperature (degrees celsius)  
 $V$ : velocity (m/s)  
 $z$ : axial coordinate (m)  
 $\alpha$ : monolith porosity factor (-)  
 $\lambda_x, \lambda_y, \lambda_z$ : thermal conductivity in the x,y,z directions ( $W/mK$ )  
 $\eta$ : viscosity ( $kg/m^2 s$ )  
 $\rho$ : density ( $kg/m^3$ )

### NON-DIMENSIONAL PARAMETERS

$Re = \rho V_z d_h / \mu$ : Reynolds number  
 $Nu = h d_h / \lambda_{fi}$ : Nusselt number  
 $Sh = m_{mi} d_h / D_{mi}$ : Sherwood Number  
 $z^+ = z / (d_h Re)$ : non-dimensional axial length

### SUBSCRIPTS

$cl$  : centerline  
 $f$  : fluid  
 $mw$  : monolith wall  
 $s$  : solid  
 $z$  : axial direction  
 $i$  : reaction identifier:  $i=1 - CO + (.5)O_2 = CO_2$   
 $i=2 - C_3H_6 + (4.5)O_2 = 3CO_2 + 3H_2O$   
 $i=3 - CH_4 + 3O_2 = CO_2 + 4H_2O$